Gravitational waves from binary black hole mergers surrounded by scalar field clouds: Numerical simulations and observational implications

Sunil Choudhary,[1] Nicolas Sanchis-Gual,[2] Anshu Gupta,[1] Juan Carlos Degollado,[3] Sukanta Bose,[1,4] and José A. Font[5,6]

[1]*Inter-University Centre for Astronomy and Astrophysics, Post Bag 4, Ganeshkhind, Pune 411 007, India*
[2]*Centro de Astrofísica e Gravitação-CENTRA, Departamento de Física, Instituto Superior Técnico-IST, Universidade de Lisboa-UL, Avenida Rovisco Pais 1, 1049-001, Portugal*
[3]*Instituto de Ciencias Físicas, Universidad Nacional Autónoma de México, México Apdo. Postal 48-3, 62251, Cuernavaca, Morelos, México*
[4]*Department of Physics & Astronomy, Washington State University, 1245 Webster, Pullman, Washington 99164-2814, USA*
[5]*Departamento de Astronomía y Astrofísica, Universitat de València, Dr. Moliner 50, 46100, Burjassot (València), Spain*
[6]*Observatori Astronòmic, Universitat de València, C/ Catedrático José Beltrán 2, 46980, Paterna (València), Spain*

(Received 14 October 2020; accepted 19 January 2021; published 16 February 2021)

We show how gravitational-wave observations of binary black hole (BBH) mergers can constrain the physical characteristics of a scalar field cloud parametrized by mass $\tilde{\mu}$ and strength ϕ_0 that may surround them. We numerically study the inspiraling equal-mass, nonspinning BBH systems dressed in such clouds, focusing especially on the gravitational-wave signals emitted by their merger-ringdown phase. These waveforms clearly reveal that larger values of $\tilde{\mu}$ or ϕ_0 cause bigger changes in the amplitude and frequency of the scalar-field-BBH ringdown signals. We show that the numerical waveforms of scalar-field-BBHs can be modeled as chirping sine-Gaussians, with matches in excess of 95%. This observation enables one to employ computationally expensive Bayesian studies for estimating the parameters of such binaries. Using our chirping sine-Gaussian signal model, we establish that observations of BBH mergers at a distance of 450 Mpc will allow to distinguish BBHs without any scalar field from those with a field strength $\phi_0 \gtrsim 5.5 \times 10^{-3}$, at any fixed value of $\tilde{\mu} \in [0.3, 0.8]$, with 90% confidence or better, in single detectors with Advanced LIGO/Virgo type sensitivities. This provides hope for the possibility of determining or constraining the mass of ultralight bosons with gravitational-wave observations of BBH mergers.

DOI: 10.1103/PhysRevD.103.044032

I. INTRODUCTION

The gravitational-wave (GW) detector network comprising the Advanced LIGO (aLIGO) and Advanced Virgo (AdV) interferometers recently launched the era of GW astronomy. The landmark observation in 2015 of a GW signal from a binary black hole (BBH) merger and the subsequent additional detections of binary mergers that followed during the first two observational campaigns (O1 and O2), including a binary neutron star (BNS) system [1], have put GW astronomy on a very firm footing. Moreover, during O3 GW candidate events have been released as public alerts to facilitate the rapid identification of electromagnetic or neutrino counterparts, expanding the capabilities of multimessenger astronomy. A significant number of candidates have been publicly announced on the GW candidate event database [2] and some confirmed detections have already been published [3–7].

Accurate computations of the gravitational waveform of a compact binary coalescence event, especially in the early inspiraling stage, yield a plethora of information about the binary and the physics of its components. While large banks of waveforms are available for BBHs, BNS mergers, and BH-NS systems, relatively less information is available about possible departures from those waveforms if the binary components were exotic (yet physically plausible) compact objects, e.g., boson stars, Proca stars, gravastars, fuzzballs, or wormholes. However, there are ongoing theoretical efforts to investigate them [8–13]. In particular, the merger of binary compact objects formed by fundamental bosonic fields has been explored in several works, including head-on collisions and orbital mergers of boson stars, oscillatons, and Proca stars [14–24]. The potential of GW astronomy for new discoveries might eventually shed light on the actual existence in nature of these theoretical proposals.

Using GW observations as probes of new physics is challenging, but they also provide a brand new experimental channel to try and find answers to the biggest unsolved

problems in fundamental physics (see, e.g., Ref. [25]). Some of these are the nature of dark matter and dark energy, the physics in the early Universe, and possible extensions of the Standard Model. A well-known example for physics beyond the Standard Model is provided by ultralight bosonic particles. The masses of the ultralight bosons of the string axiverse can range from 10^{-33} to 10^{-10} eV [26]. Even though their masses can be smaller than those of known particles, their existence is possible if the coupling to ordinary matter is very weak.

In particular, scalar fields surrounding supermassive BHs in galactic centers have been proposed as candidates for dark matter [27–31]. This model assumes that dark matter is composed of bosonic particles that may condense into macroscopic objects around BHs. The justification for this proposal requires long-lived scalar-field configurations. Their dynamics and lifetime have been studied both in the linear regime [32–36] and with nonlinear simulations in general relativity [37–39], providing convincing support to the proposal. Specifically, the early work in Ref. [34] in the linearized regime showed that *massive* scalar fields surrounding stationary and *nonrotating* BHs could indeed form such quasibound states as a result of the presence of a potential well due to the mass term. These states decay at infinity and are characterized by a complex frequency whose real part represents the actual oscillation frequency, while the imaginary part gives (depending on the sign) either their decay rate or the growth rate, if a mode is superradiantly unstable.

The superradiant instability operates in *rotating* black holes (but see Ref. [40] for an academic setup with a Reissner-Nordström BH) where bosonic waves scattered off the BH extract energy and angular momentum and increase the energy of the field through the classical process of superradiance [41,42] (see also Ref. [43] and references therein). The nonlinear realization of superradiance in Kerr BHs was recently shown in Refs. [44,45] by employing a vector (Proca) bosonic field (see also Refs. [46,47]). The end state of this process is the formation of *hairy* BHs, i.e., Kerr BHs surrounded by either scalar or vector hair, in which the bosonic field is in equilibrium (i.e., synchronized) with the BH [48,49]. Recent works [50–59] have investigated possible observational signatures of the bosonic clouds through the detection of the nearly monochromatic GWs they emit, providing procedures to, e.g., constrain the QCD axion [50], probe ultralight bosons in BBH inspirals through the analysis of resonant transitions between growing and decaying modes of the clouds [54], and estimate upper limits for the detectability of ultralight bosons through direct GW searches [51,53]. Recent attempts [59] promoted the use of third-generation ground-based GW detectors combined with the spaced-based LISA mission to increase the chances of detection using a multiband technique. We also note that the direct detection of bosonic fields in the form of bosonic stars has been recently proposed in connection with GW190521 [60]. Last, for its relevance to our setup and results, we highlight the work of Ref. [52] which investigated the joint evolution of intermediate-mass BBHs surrounded by a shell of an axion-like scalar field of different strengths, finding that the dynamics of the mergers can be modified by the presence of the environmental scalar field cloud, which also impacts the GW emission.

In this work we also investigate if GW measurements can probe the existence of bosonic clouds around BHs but we employ a different setup to that used in most previous works. We study if the presence of a scalar field cloud might actually be established through its imprint on the GWs from BBH mergers. Our goal is to show through a combination of numerical-relativity simulations and Bayesian inference if the actual network of GW interferometers can measure the differences in the waveforms induced by the presence of scalar field clouds around the coalescing BHs. To this aim we parametrize the cloud by its mass $\tilde{\mu}$ and strength ϕ_0. Our investigation reveals that it may actually be possible to observationally distinguish BBHs without any scalar field from those with a field strength of order $\phi_0 \gtrsim 5.5 \times 10^{-3}$, at any fixed value of $\tilde{\mu} \in [0.3, 0.8]$, with 90% confidence or better, in single detectors with aLIGO or AdV type sensitivity, up to distances of about 450 Mpc. At smaller distances (∼100–200 Mpc) even weaker fields might be distinguishable.

This paper is organized as follows. In Sec. II we briefly summarize our basic framework to study the dynamics of BBH mergers endowed with bosonic clouds. Section III describes the numerical setup, initial data, and results of the numerical simulations for varying scalar-field parameters. The measurement and estimation of these parameters through Bayesian inference are discussed in Sec. IV, and we close with Sec. V which presents our conclusions. Appendix B provides specific details on our numerical waveforms. Throughout the paper we use natural units, $c = G = \hbar = 1$.

II. BASIC FRAMEWORK

Our approach to modeling BBH mergers surrounded by a scalar field environment considers a massive complex scalar field interacting through gravity with the BHs. The system is governed by the Einstein-Klein-Gordon theory. Details of the formulation have been given in Refs. [37,61], which we briefly summarize here. We consider a complex scalar field Φ minimally coupled to gravity described by the action

$$S = \int d^4x\sqrt{-g}\left(\frac{1}{16\pi}R - \frac{1}{2}g^{\alpha\beta}\nabla_\alpha\Phi^*\nabla_\beta\Phi - \frac{1}{2}m_s^2\Phi\Phi^*\right), \tag{1}$$

where R is the Ricci scalar associated with the metric $g_{\alpha\beta}$ with determinant g and m_s is the mass of the field.

The asterisk indicates the complex-conjugate operation and ∇_α denotes the covariant derivative. Minimizing this action with respect to the metric and scalar field yields the Einstein-Klein-Gordon system:

$$R_{\alpha\beta} - \frac{1}{2} g_{\alpha\beta} R = 8\pi T_{\alpha\beta} \tag{2}$$

and

$$g^{\alpha\beta}\nabla_\alpha\nabla_\beta\Phi = m_s^2\Phi, \tag{3}$$

where $T_{\alpha\beta}$ is the stress-energy tensor

$$T_{\alpha\beta} = \frac{1}{2}(\nabla_\alpha\Phi\nabla_\beta\Phi^* + \nabla_\alpha\Phi^*\nabla_\beta\Phi) - \frac{1}{2} g_{\alpha\beta}(g^{\gamma\sigma}\nabla_\gamma\Phi\nabla_\sigma\Phi^* + m_s^2\Phi\Phi^*). \tag{4}$$

In this setup, the self-gravitating scalar field interacts with the binary through gravity by means of the spacetime metric described by the Einstein equations.

Given the total Arnowitt-Deser-Misner mass M of a gravitational system, we define the dimensionless parameter

$$\tilde{\mu} \equiv \frac{GMm_s}{\hbar c} \tag{5}$$

to characterize the scalar cloud. This parameter is the ratio of the gravitational radius of the system $R_g = GM/c^2$ and the Compton wavelength of the scalar field $\lambda_c = \hbar/(m_s c)$.

The linear dynamics of scalar fields propagating on a single, nonrotating BH background has been described in [62]. It was found that regular scalar field configurations in the form of quasibound states around Schwarzschild BHs may survive in the vicinity of the compact objects for a certain range of values of the scalar field and BH masses. A detailed analysis of the scalar field configurations including the spectrum of quasibound states can be found in Ref. [63].

The description of the scalar field assumes a harmonic time dependence, $\Phi(t,\vec{r}) = \phi(\vec{r})e^{-i\omega t}$, where ω is a complex number whose real part indicates the oscillating frequency and whose imaginary part determines the decay rate of the field. For small values of the dimensionless parameter $\tilde{\mu}$ it was found that the decay rate of the quasibound states decreases as a power law of $\tilde{\mu}$. The mass spectrum of axion-like particles that could be probed for a given coupling $\tilde{\mu}$ is continuous, and includes, among others, the QCD axion and a large range of particles beyond the Standard Model predicted in the string axiverse scenario [26]. We highlight in particular two regimes with astrophysical relevance for the combination of the scalar field and BH masses for which the scalar field configurations may live around the central object for longer times than the age of the Universe. The first one occurs when the scalar field mass is of the order of 1 eV and the BH has a mass smaller than $10^{-17}\ M_\odot$. The second regime corresponds to an ultralight scalar field with mass smaller than 10^{-22} eV and to a supermassive BH with mass smaller than $5\times10^{10}\ M_\odot$. These scenarios correspond, respectively, to axion distributions of a scalar field around primordial BHs and dark matter halos around supermassive BHs in the centers of galaxies [64]. For stellar-size BHs (like the ones employed in this work) with mass $\sim 40\ M_\odot$, the mass of the particle corresponds to $\sim 10^{-12}$ eV.

III. NUMERICAL SIMULATIONS

In order to write Eqs. (2) and (3) as an evolution system suitable for numerical integration we formulate the Einstein-Klein-Gordon system using the BSSN formulation [65–67] (see also Refs. [68,69]). Our numerical simulations are performed using the open source EinsteinToolkit infrastructure [70–72]. In addition, the Carpet package [73,74] is used for mesh-refinement capabilities, BH apparent horizons are found using AHFinderDirect [75,76], and the left-hand side of the Einstein equations is solved using the MacLachlan code [77]. The scalar-field evolution code is our own modification of the publicly available Proca thorn from the Canuda library [78,79] to evolve complex scalar fields. This code has been recently employed to study the stability of spinning bosonic stars [80,81]. The method of lines with a fourth-order Runge-Kutta scheme is employed to integrate the time-dependent differential equations.

A. Initial data

To set initial data suitable for numerical evolution using the moving punctures technique we take advantage of the Bowen-York construction for two BHs in vacuum [82]. Thus, a nontrivial analytic solution of the momentum constraint equation can be found [83] and the Hamiltonian constraint equation can be solved using the puncture approach [84–86]. Once the Hamiltonian and momentum constraints are solved we introduce a nonzero scalar field distribution. The addition of the scalar field to the binary system introduces violations of the constraints (see details in Appendix A). However, our results regarding GW emission show that the initial violation produces only a weak spurious GW signal as long as the amplitude of the scalar field $\phi_0 \ll 1$ for $\tilde{\mu} \approx 1.0$.

In our study we mainly focus on the post-merger characteristics of the gravitational waveforms. Therefore, for simplicity we initiate our simulations when the two BHs are in their last orbit prior to merger using initial data for a quasicircular orbit [87,88]. The BHs are positioned at $(x,y,z) = (-1.168M, 0, 0)$ and $(1.168M, 0, 0)$, having linear momentum vectors $(0, -0.333M, 0)$ and $(0, 0.333M, 0)$.

Our simulations are performed for a nonspinning, equal-mass ($m_1 = m_2 = 0.453M$) BBH system which is surrounded by a scalar field cloud initially shaped in the form of a Gaussian distribution, $\Phi = \phi_0 e^{-(r-r_0)^2/\lambda^2}$, centered at radius $r_0 = 0$, where ϕ_0 is the initial amplitude and λ is its half-width. We simulate a series of configurations by varying the amplitude ϕ_0 between 1.0×10^{-5} and

1.0×10^{-2} and employing a dimensionless scalar field mass parameter $\tilde{\mu} < 1.0$. We have observed that due to the choice of constraint-violating conditions caused by the presence of the cloud, numerical inaccuracies dominate the evolution of the system for values of $\tilde{\mu}$ of order 10^{-2}. Therefore, such values are not considered. On the other hand, high-amplitude fields ($\phi_0 \approx 0.01$) trigger their collapse inside the horizon, while very low-amplitude fields ($\phi_0 < 5.0 \times 10^{-4}$) lead to evolutions that are almost indistinguishable from the pure vacuum BBH case. Keeping this in mind, we simulate a fiducial number of 18 configurations, setting the scalar field mass parameter $\tilde{\mu}$ in the range from 0.3 to 0.8 for three scalar field amplitudes, namely, $\phi_0 = 3.5 \times 10^{-3}$, 4.5×10^{-3}, and 5.5×10^{-3}. These simulations are compared with the vacuum BBH merger case in the absence of any scalar field.

The mass of the cloud is kept sufficiently small compared to the total BBH mass to ensure that the violation of the constraints does not represent a major drawback of our initial data. For rotating BHs there is a mechanism (superradiance) that allows the cloud to grow up to about 10% of the mass of the BH. We take this value as an upper bound for the mass of the cloud (which scales quadratically with ϕ_0) assuming there is no other mechanism to grow the cloud. In addition, we choose $\lambda = 15$ which yields a size for the scalar cloud comparable to the physical size of the BHs. Much larger values of λ correspond to cloud masses that would result in significant constraint violation in our numerical evolution. Much smaller values (that are still larger than the gravitational radius of the system) would require large field amplitudes to leave any noticeable imprint in the merger waveforms. The effect of varying λ, along with the contribution of the inspiral part of the GW signal in our results, will be explored in more detail in a future work.

The numerical evolutions are performed on a Cartesian grid with a domain size of $(-320M, 320M)$ for all three dimensions. However, we apply reflection symmetry in the z direction; thus, the computational domain in that direction is $(0, 320M)$. The numerical grid has nine refinement levels, starting with two centers located at each puncture, and with resolution $\{(320, 160, 80, 40, 20, 5, 2.5, 1.25, 0.625)M, (8, 4, 2, 1, 0.5, 0.25, 0.125, 0.0625)M\}$. The first set of numbers indicates the spatial domain of each level and the second set indicates the resolution.

B. Results of the numerical evolutions

Our goal is to highlight possible imprints of the presence of scalar field clouds in the gravitational waveforms produced during a BBH merger. GW signals are obtained from the simulations by computing the Newman-Penrose scalar Ψ_4 defined in terms of the Weyl tensor $C_{\alpha\beta\gamma\delta}$ [89] as

$$\Psi_4 = C_{\alpha\beta\gamma\delta} k^\alpha \bar{m}^\beta k^\gamma \bar{m}^\delta, \tag{6}$$

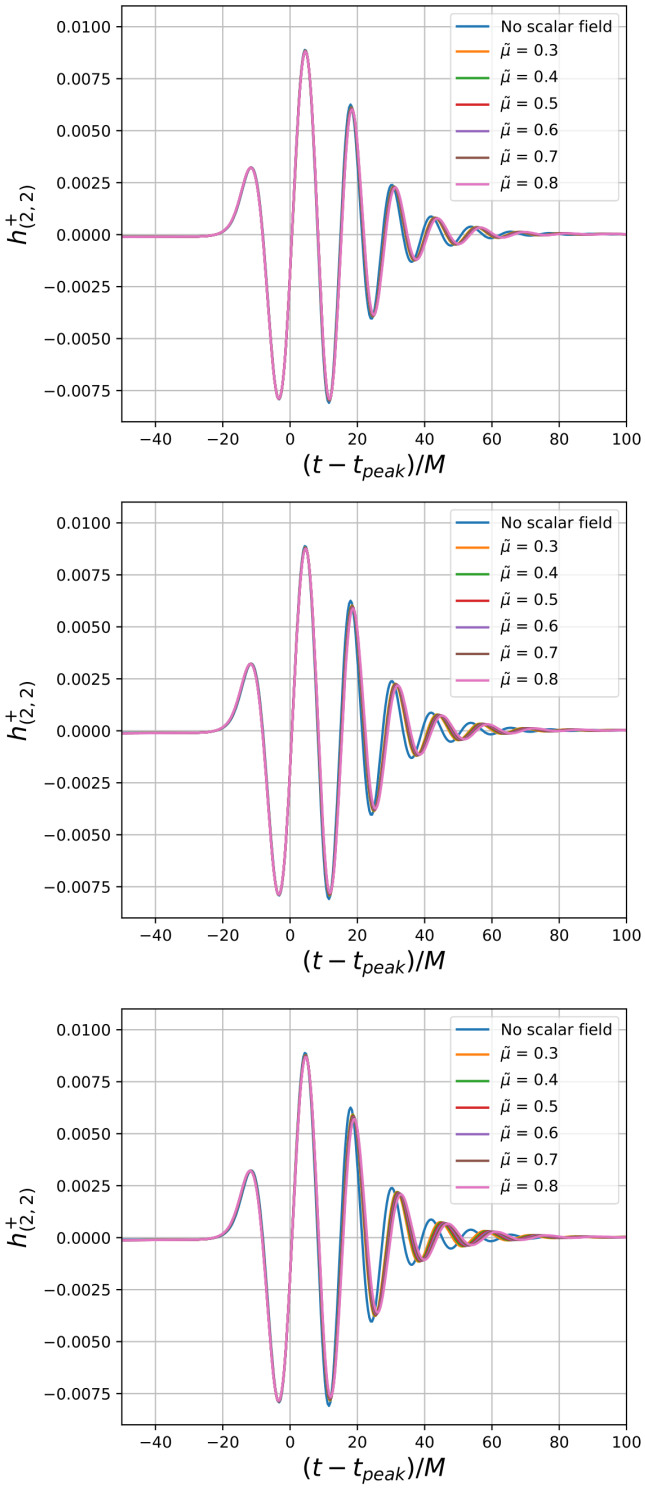

FIG. 1. $l = m = 2$ mode of the real part of the GW strain h_+ extracted at $r_{\rm ext} = 40M$. Different curves correspond to varying values of the scalar field mass parameter $\tilde{\mu}$ for the field amplitudes $\phi_0 = 3.5 \times 10^{-3}$ (top panel), $\phi_0 = 4.5 \times 10^{-3}$ (middle panel), and $\phi_0 = 5.5 \times 10^{-3}$ (bottom panel).

where k and $\bar{m}$ are two components of the null tetrad l, k, m, $\bar{m}$ that satisfy $\ell \cdot k = -1$ and $m \cdot \bar{m} = 1$, and all other inner products are zero. At a given extraction radius $r_{\rm ext}$ we

perform a multipolar decomposition by projecting Ψ_4 onto a spherical harmonic basis of spin weight $s = -2$ as

$$\Psi_4(t, r, \theta, \varphi) = \sum_{\ell,m} \psi_4^{\ell,m}(t, r)\, {}_{-2}Y_{\ell,m}(\theta, \varphi), \tag{7}$$

whose relation with the second time derivative of the two polarizations of the GW strain is given by

$$\psi_4^{\ell,m}(t, r) = \ddot{h}^{+}_{\ell,m} - i\ddot{h}^{\times}_{\ell,m}. \tag{8}$$

We use the post-processing Python package pyGWAnalysis [90] to convert Ψ_4 data to GW strain. Figure 1 displays the real part of the dominant quadrupolar ($l = m = 2$) mode of the GW strain (h^+) for varying values of the mass of the scalar field and its initial amplitude. The signal is extracted at $r_{\rm ext} = 40M$ and $t_{\rm peak}$ refers to the instant of time when the norm of the strain waveform $|h_{2,2}|$ reaches its maximum. This figure shows that the presence of the scalar field produces a shift in the signal compared to the vacuum BBH case. This shift is most visible in the ringdown part of the signal and becomes larger the larger the values of $\tilde{\mu}$ and ϕ_0.

The stronger and faster damping observed during the ringdown in the presence of high-amplitude scalar fields is highlighted in Fig. 2. This figure compares the waveforms for $\phi_0 = 3.5 \times 10^{-3}$ and 5.5×10^{-3}, both for $\tilde{\mu} = 0.5$, with a BBH merger with no scalar field content. In order to quantify this effect and to study the distinguishability of ϕ_0 in actual GW observations, we carry out Bayesian inference with our waveform models. This is discussed in the next section.

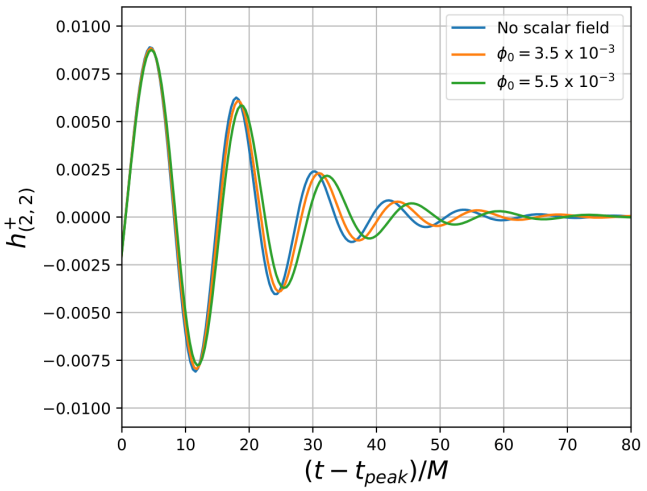

FIG. 2. Comparison of the ringdown quadrupolar GW strains of BBH mergers with and without scalar field content. The former corresponds to the $\tilde{\mu} = 0.5$ case with $\phi_0 = 3.5 \times 10^{-3}$ and 5.5×10^{-3}. The labels here are the same as in Fig. 1.

IV. MEASURING SCALAR FIELD PARAMETERS IN OBSERVATIONS OF BBH MERGERS

With multiple BBH merger detections in the past and several tens to hundreds expected from ground-based detectors in the coming years, it will likely become possible to distinguish BBHs with sufficiently large scalar field amplitudes from those without any such field, or at least constrain the presence of such fields in BBH mergers. To estimate how precisely one will be able to do so, we fitted several models to the post-merger parts of our numerical-relativity waveforms, out of which the chirp sine-Gaussian waveform model came out to be the most suitable one, partly motivated by the exponentially damped sinusoid nature of the signal in the absence of a scalar field (see, e.g., Refs. [91,92] and references therein). This is due to both its simple structure and the small number of parameters it employs, as well as its very high match ($\gtrsim$95%) with the numerical waveforms. The chirp sine-Gaussian form is described by the GW strain

$$g(t; f_0, Q, \kappa) \equiv A e^{-4\pi^2 f_0^2 t^2/Q^2} \cos(2\pi f_0 t + \kappa t^2), \tag{9}$$

where Q is the quality factor that dictates the damping time, f_0 is the central frequency of the sinusoid, and κ is the "chirp parameter" quantifying the rate of change of frequency with time (see Ref. [93] for details).

A. Bayesian parameter estimation

To assess how well the analytical model of our ringdown signals in Eq. (9) matches the numerical waveforms, and the precision as well as accuracy with which one can measure the BBH and scalar field parameters, we use Bayesian inference. The code employed to implement it on our simulated detector data and signals is Bilby [94], which is primarily designed for inferring the parameters of compact binary coalescence signals. It provides both nested sampler and Markov chain Monte Carlo sampler options for computing the parameter posteriors of modeled waveforms. In our study we use the nested sampler "Dynesty" [95,96] since it is a more appropriate choice when only a few parameters characterize a large set of waveforms.

To perform this Bayesian analysis, the numerical waveforms are scaled such that for each set of parameter error estimates the source is always kept at a fixed distance, namely, at 450 Mpc. Increasing the source distance leads to an increase in parameter errors that can make it difficult to distinguish the scalar-field values simulated here.

We use the IMRPhenomD waveform templates [97,98] with the lower-frequency cutoff set high enough in our analysis so as to utilize only the post-merger parts of the signals for computing the signal-to-noise ratios (SNRs) and parameter estimates. In particular, parameter estimation is performed using the quadrupolar ($l = m = 2$) mode of the GW strain waveform, as described in Sec. III B.

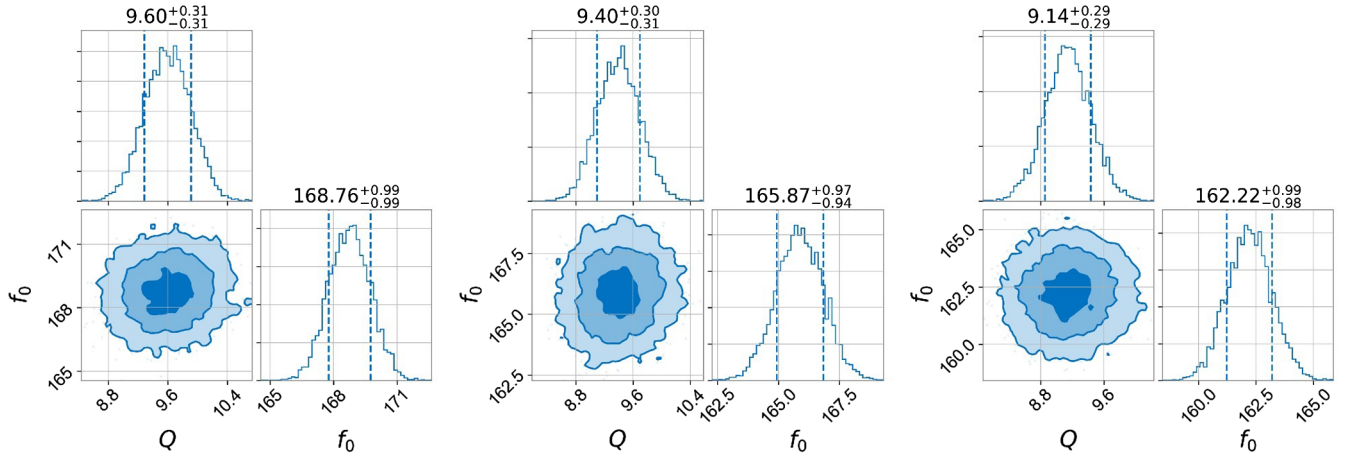

FIG. 3. Corner plots showing the posterior distributions of f_0 and Q of our chirp sine-Gaussian waveform model for $\phi_0 = 3.5 \times 10^{-3}$ (left), $\phi_0 = 4.5 \times 10^{-3}$ (middle), and $\phi_0 = 5.5 \times 10^{-3}$ (right). All three cases correspond to $\tilde{\mu} = 0.50$.

We truncate every waveform such that only the cycles following the peak amplitude are retained. All waveforms are injected in simulated zero-mean, colored Gaussian noise using aLIGO's zero-detuned-high-power noise power spectral density [99]. The time axis of the numerical waveform is scaled by setting up the component masses such that the signal frequency lies in the aLIGO sensitivity band. The component masses that we need for this purpose are of the order of 40 $M_\odot$ and the mass of the scalar particle is in the range between 0.5×10^{-12} and 1.4×10^{-12} eV. Further details about the procedure are provided in Appendix B.

The priors used for the parameters Q and f_0 are uniform, with $Q \in [6, 14]$ and $f_0 \in [140, 190]$ Hz, and the likelihood used is Gaussian with sigma set equal to the standard deviation of aLIGO noise. The posteriors thus calculated give us the estimated values and the 1σ error bars. Some illustrative corner plots of these posteriors are shown in Fig. 3. As mentioned before, we consider three scalar-field cases with $\tilde{\mu}$ ranging from 0.3 to 0.8. In physical units this corresponds to 0.7×10^{-12}–1.8×10^{-12} eV for BBHs with each component of the order of 30 $M_\odot$ and to 3.4×10^{-13}–9×10^{-13} eV for BBHs with 60 $M_\odot$ components.

The κ parameter is fixed to 13 000 Hz^2 in all cases as we observed that it does not vary much for different values of ϕ_0 and $\tilde{\mu}$. It only shows a variation of 15% when set free but does not have much of an effect on the match (which changes by <1%). Lists of estimated parameters are shown in Tables I and II for source distances of 100 and 450 Mpc, respectively.

By studying injections at very high SNRs, we confirmed that the systematic error in the estimated parameters—in particular f_0 as listed in Table I (where the source distance is taken at 100 Mpc)—is no more than ∼0.1%. With these estimated parameters our model gives a more than 99% match with the post-merger part of the waveform, as shown in Fig. 4 for the particular case $\phi_0 = 5.5 \times 10^{-3}$ and $\tilde{\mu} = 0.5$.

To validate our parameter estimation method we perform some tests by checking how accurately it estimates the parameters f_0, Q, and κ of simulated chirping sine-Gaussian signals. For this purpose, we vary κ from

TABLE I. Variation in medians and 90% errors in Q and f_0 with ϕ_0 and $\tilde{\mu}$. Here $\tilde{\mu}$ varies from 0.3 to 0.8 for three values of the scalar field: $\phi_0 = 3.5 \times 10^{-3}$, 4.5×10^{-3}, and 5.5×10^{-3}. The error bars are for a source distance of 100 Mpc. These variations are plotted in Figs. 6 (left panel) and 7.

Best parameter fits for 100 Mpc		
ϕ_0 and $\tilde{\mu}$	Q	f_0 (Hz)
0; 0 (no scalar field)	9.89^{+34}_{-32}	$173.54^{+0.98}_{-0.94}$
Case $\phi_0 = 3.5 \times 10^{-3}$		
0.30	$9.66^{+0.32}_{-0.32}$	$169.76^{+0.96}_{-0.99}$
0.40	$9.62^{+0.31}_{-0.31}$	$169.25^{+0.93}_{-0.94}$
0.50	$9.60^{+0.31}_{-0.31}$	$168.76^{+0.99}_{-0.99}$
0.60	$9.56^{+0.30}_{-0.30}$	$168.28^{+0.96}_{-0.95}$
0.70	$9.53^{+0.30}_{-0.31}$	$167.83^{+0.94}_{-1.00}$
0.80	$9.51^{+0.30}_{-0.32}$	$167.21^{+0.96}_{-1.01}$
Case $\phi_0 = 4.5 \times 10^{-3}$		
0.30	$9.51^{+0.31}_{-0.30}$	$167.39^{+0.94}_{-0.95}$
0.40	$9.47^{+0.31}_{-0.31}$	$166.52^{+0.95}_{-0.92}$
0.50	$9.40^{+0.30}_{-0.30}$	$165.87^{+0.97}_{-0.94}$
0.60	$9.34^{+0.31}_{-0.30}$	$165.06^{+0.95}_{-0.96}$
0.70	$9.28^{+0.31}_{-0.29}$	$164.24^{+0.99}_{-0.96}$
0.80	$9.22^{+0.28}_{-0.29}$	$163.35^{+0.93}_{-0.98}$
Case $\phi_0 = 5.5 \times 10^{-3}$		
0.30	$9.32^{+0.29}_{-0.31}$	$164.43^{+0.92}_{-0.96}$
0.40	$9.23^{+0.28}_{-0.30}$	$163.26^{+0.96}_{-1.02}$
0.50	$9.14^{+0.29}_{-0.29}$	$162.22^{+0.99}_{-0.98}$
0.60	$9.06^{+0.28}_{-0.29}$	$161.16^{+0.96}_{-0.99}$
0.70	$8.99^{+0.28}_{-0.30}$	$159.87^{+0.97}_{-0.94}$
0.80	$8.89^{+0.28}_{-0.28}$	$158.48^{+0.96}_{-0.95}$

TABLE II. Variation in medians and 90% errors in f_0 with ϕ_0 and $\tilde{\mu}$ for a source distance of 450 Mpc. These variations are plotted in the right panel of Fig. 6. The values for the parameter Q are not included in the table as their error bars overlap with the no-scalar-field case.

Best parameter fits for 450 Mpc	
ϕ_0 and $\tilde{\mu}$	f_0 (Hz)
0; 0 (no scalar field)	$174.00^{+4.19}_{-4.34}$
Case $\phi_0 = 4.5 \times 10^{-3}$	
0.30	$168.10^{+4.44}_{-4.22}$
0.40	$167.29^{+4.45}_{-4.41}$
0.50	$166.67^{+4.60}_{-4.45}$
0.60	$165.81^{+4.49}_{-4.38}$
0.70	$165.00^{+4.52}_{-4.39}$
0.80	$164.10^{+4.70}_{-4.50}$
Case $\phi_0 = 5.5 \times 10^{-3}$	
0.30	$165.29^{+4.39}_{-4.31}$
0.40	$164.08^{+4.56}_{-4.42}$
0.50	$163.14^{+4.45}_{-4.48}$
0.60	$162.14^{+4.60}_{-4.61}$
0.70	$160.95^{+4.54}_{-4.58}$
0.80	$159.65^{+4.65}_{-4.72}$

12 000 to 14 700 Hz^2 in steps of 300 Hz^2. We do this for two cases. In the first case we fix $f_0 = 157.0$ Hz, $Q = 9.2$ and in the second case we fix $f_0 = 145.0$ Hz, $Q = 8.6$. The results, shown in Fig. 5, demonstrate the effectiveness of our method in recovering the signal parameters.

B. Revealing scalar field properties by measuring f_0

The signal parameter f_0 is an accurate tracker of the strength of the scalar field ϕ_0, so long as we allow for its variation with the parameter $\tilde{\mu}$. It is worth mentioning that

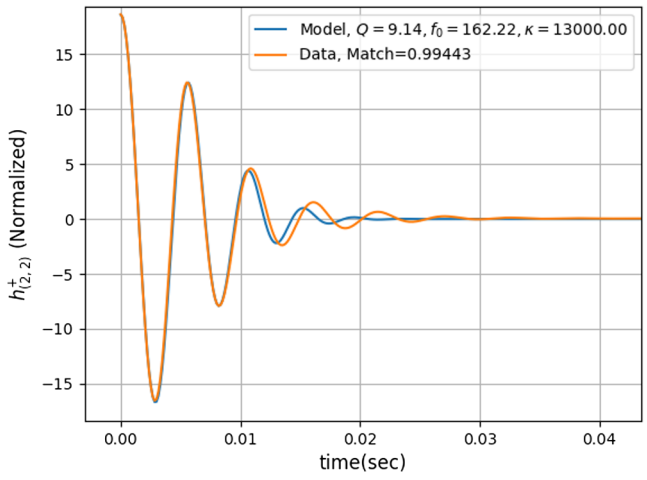

FIG. 4. Comparison of the post-merger waveform against the chirp sine-Gaussian fitted model for the case $\phi_0 = 5.5 \times 10^{-3}$ and $\tilde{\mu} = 0.5$. It yields more than a 99% match.

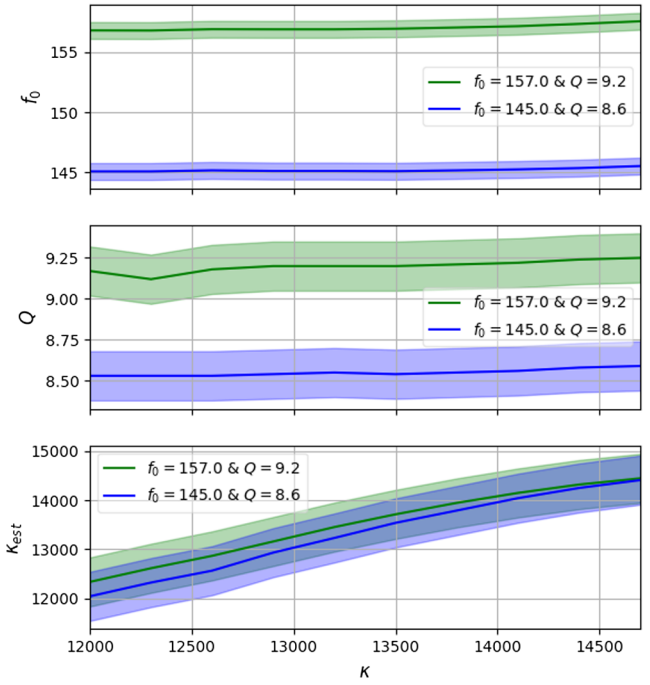

FIG. 5. Results of our validation study for f_0 (top), Q (middle), and $\kappa_{\rm est}$ (bottom) for varying values of κ.

for a fixed value of $\tilde{\mu}$, as the value of ϕ_0 increases the mass of the scalar field cloud grows. We use the chirping sine-Gaussian templates in Bilby, as given by Eq. (9), to measure the values of f_0 and Q for the multiple numerical-relativity waveforms simulated for various scalar field configurations. Specifically, we perform parameter estimation for our three values of ϕ_0, namely, 3.5×10^{-3}, 4.5×10^{-3}, and 5.5×10^{-3}, as well as for our six values of $\tilde{\mu}$ ranging from 0.3 to 0.8. This range of values of ϕ_0 allows us to study scalar clouds having less than 10–15% of the mass of the binary.

Figures 6 and 7 show the variation of the model parameters f_0 and Q, respectively, with the numerical waveform parameter $\tilde{\mu}$. The closer the source the better the results. If the source is at 100 Mpc (left panels of Figs. 6 and 7), for which the match-filtering SNR value using the post-merger part of template is ≈210, the error bars in the measurements of Q overlap for our choices of scalar field strengths. However, the error bars in f_0 are separate and all of the 18 cases considered can be distinguished from one another, and from the no-scalar-field case (with error and median values shown in Table I).

We note that even if the source is at a distance of 200 Mpc, one finds that the error bars for f_0 remain separable for much of the $\tilde{\mu}$ range studied here. However, at larger source distances the situation worsens and it is only possible to distinguish stronger scalar fields from the no-scalar-field BBH mergers. This is shown in the right panel of Fig. 6 for a source located at 450 Mpc for which the match-filtering SNR value using the post-merger part of

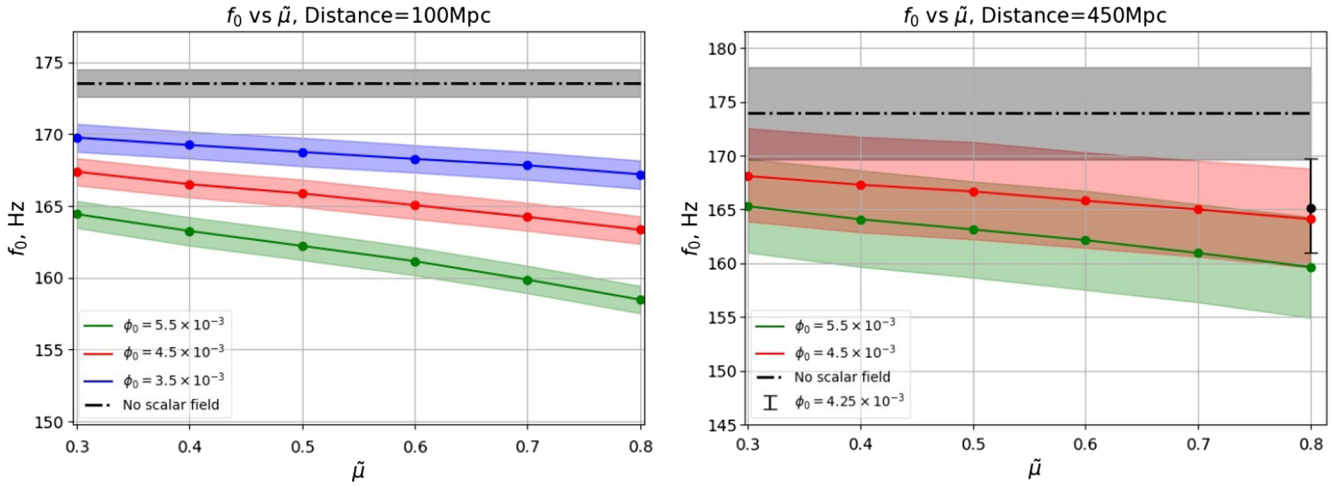

FIG. 6. Left: medians and 1σ error regions (with interpolations) of the f_0 posteriors plotted as functions of $\tilde{\mu}$ for the three values of ϕ_0 and for a source located at a distance of 100 Mpc. The filled circles denote the values of $\tilde{\mu}$ where the posteriors were individually computed. The value of f_0 for the no-scalar-field case is $173.54^{+0.98}_{-0.94}$ Hz and is shown as a horizontal line in the plot for reference. Right: f_0 vs $\tilde{\mu}$ for a source distance of 450 Mpc. The frequency estimate for the no-scalar-field case, $f_0 = 174.0^{4.19}_{4.34}$, cannot be distinguished from the estimate for the $\phi_0 = 3.5 \times 10^{-3}$ case for $\tilde{\mu} < 0.7$; it can, however, be distinguished from the $\phi_0 = 4.5 \times 10^{-3}$ case for all $\tilde{\mu}$ except those close to 0.3. The figure also shows that the $\phi_0 = 4.25 \times 10^{-3}$ case is the limiting value of ϕ_0 that can be distinguished from the no-scalar-field case, close to $\tilde{\mu} = 0.8$.

template is ≈45, a distance around or above the values at which most GW signals from BBH coalescence events are observed by the Advanced LIGO and Advanced Virgo detector network.

With the previous results we can attempt to fit f_0 as a function of $\tilde{\mu}$,

$$f_0(\tilde{\mu}) = a\tilde{\mu} + b. \tag{10}$$

The fits corresponding to the different values of ϕ_0 for the source at a distance of 100 Mpc are plotted in Fig. 8. Values of the coefficients a and b are listed in Table III. As can be seen from the fits (Table III) and Figs. 6 and 8, the frequency f_0 shows a clear dependence on ϕ_0 and $\tilde{\mu}$ and its measurement can be used to put bounds on the characteristics of the source.

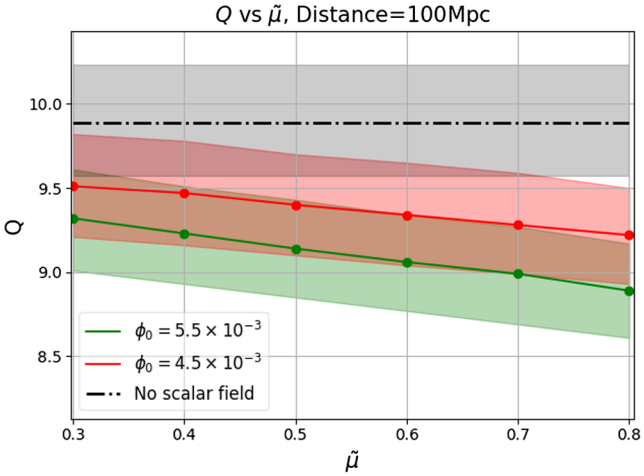

FIG. 7. Median and 1σ error regions of the Q posteriors as a function of $\tilde{\mu}$ for $\phi_0 = 5.5 \times 10^{-3}$ and $\phi_0 = 4.5 \times 10^{-3}$ and for a source at a distance of 100 Mpc. The value of Q for the no-scalar-field case is 9.89^{+34}_{-32}.

To quantify it further, in Fig. 9 we plot isocontours of $f_0(\tilde{\mu}, \phi_0)$. An isocontour of f_0 specifies the region of the parameter space that is allowed by the measured value of f_0. For example, if an observed GW signal has a frequency $f_0 = 166$ Hz, then this implies that in the range $\tilde{\mu} \in [0.3, 0.8]\phi_0$ must lie between $\sim 3.8 \times 10^{-3}$ and $\sim 5.0 \times 10^{-3}$. Since the measured f_0 value will typically lie in a confidence interval, the range of ϕ_0 will also have a corresponding spread. Furthermore, if the value of Q can be measured as well with some precision, then along with f_0 it will provide a measurement of the important quantity $\tilde{\mu}$ characterizing the scalar field cloud. As suggested by Fig. 7, this result might be elusive unless we detect a golden binary with a large SNR.

TABLE III. Coefficients of the fitting model f_0, described by Eq. (10), for the three values of the scalar field $\phi_0 = 3.5 \times 10^{-3}$, 4.5×10^{-3}, and 5.5×10^{-3} at 100 Mpc, are listed here.

Model coefficients		
ϕ_0	a (Hz)	b (Hz)
0.0035	−5.0	171.3
0.0045	−8.0	169.8
0.0055	−11.7	168.0

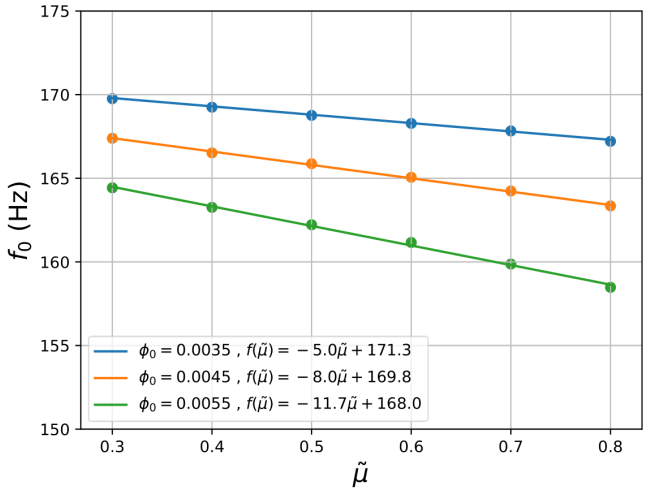

FIG. 8. Linear fits for f_0 as a function of $\tilde{\mu}$, $f_0(\tilde{\mu}) = a\tilde{\mu} + b$, for our three values of ϕ_0.

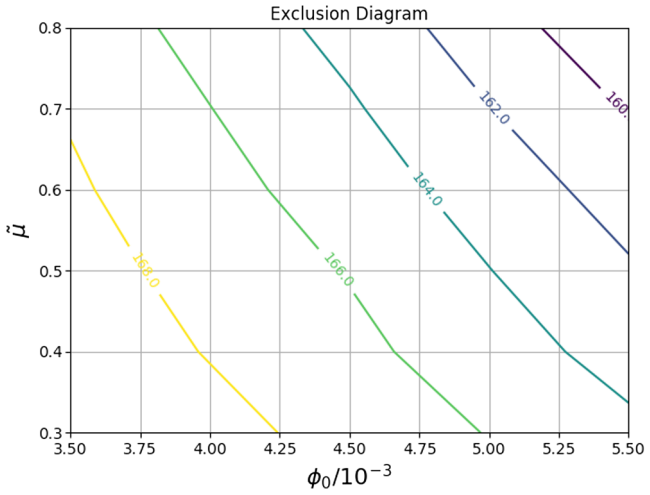

FIG. 9. Isocontours of f_0 in the $\phi_0 - \tilde{\mu}$ plane for a source at 100 Mpc.

V. CONCLUSIONS

Massive scalar fields surrounding stationary and nonrotating BHs can form long-lived, quasibound states, or clouds, as a result of the presence of a potential well due to the mass term [63]. For rotating BHs, the superradiant instability [43] leads to the formation of hairy BHs—Kerr BHs surrounded by bosonic (scalar or vector) hair in which the frequency of the field is synchronized with the angular velocity of the BH [48,49]. Using numerical-relativity simulations, we have studied mergers of BBH systems dressed in such scalar field clouds. Our aim has been to find out whether GW observations of BBH mergers could constrain the physical characteristics of a scalar field cloud surrounding these compact binaries. We have considered equal-mass BBH systems endowed with Gaussian distributions of scalar field clouds parametrized by their mass $\tilde{\mu}$ and strength ϕ_0, and analyzed the imprints on the GWs generated during the mergers. We have numerically simulated the last three quarters of the final orbit prior to merger for a large set of initial models, restricting our analysis to the post-merger phase.

The waveforms extracted from our simulations have revealed that larger values of $\tilde{\mu}$ or ϕ_0 cause bigger changes in the amplitude and frequency of the ringdown part of the signals. The ringdown signals of our mergers can be simulated analytically as chirping sine-Gaussians, characterized by only three parameters, returning match values with our numerical-relativity waveforms in excess of 95%. This is not surprising since BBH ringdown signals in general relativity are damped sinusoids that can be modeled with only two parameters [100]. Using our chirping sine-Gaussian signal model, we have carried out computationally expensive Bayesian studies for estimating the parameters of BBH binaries endowed with scalar field clouds. We have been able to establish that the central frequency of the model, f_0, has a strong dependence on the scalar-field strength ϕ_0 and a weak dependence on $\tilde{\mu}$. Therefore, at a fixed value of $\tilde{\mu}$, a measurement of the signal parameter f_0 leads to a measurement of ϕ_0. In particular, we have shown that it is possible to distinguish BBHs without any scalar field from those with a field strength $\phi_0 = 5.5 \times 10^{-3}$, at any fixed value of $\tilde{\mu} \in [0.3, 0.8]$, from observations of BBH mergers at distances of 450 Mpc with 90% confidence or better. We have shown that aLIGO may have the potential to distinguish between (i) a GW signal produced by a BBH with component masses of 40 $M_\odot$ each in vacuum and (ii) that produced by one with the same component masses but immersed in a cloud of boson particles with masses in the range $[5 \times 10^{-13}, 1.4 \times 10^{-12}]$ eV.

We take these results as encouraging indications for the prospect of constraining scalar field clouds in BBH observations. However, to assess their utility for real observations one must study the impact of a wider parameter space of the binaries on how accurately and precisely one will be able to measure the scalar-field parameters from the waveforms, while also battling possible parameter degeneracies that can arise. For instance, the same f_0 and Q values can correspond to a variety of BBH remnant masses and spins as well as scalar-field parameters. (Arguably, some of these degeneracies may break or be mitigated by measurements of source parameters in the inspiral part of the signals.) To address this issue, one will need to simulate waveforms for a broader range of astrophysically relevant BBH component masses and spins and scalar-field parameters, and analyze the parameter degeneracies that might arise as well as their possible resolution. We leave this computationally expensive study for the future.

While in this investigation we have limited ourselves to single BBH observations, we note that by combining

multiple BBH detections one may be able to constrain the scalar-field configurations in these mergers collectively for populations. Such an exercise will be similar to stacking ringdown signals from multiple BBH signals to, e.g., test the no-hair theorem. In our case, however, a straightforward extension to populations is complicated by the possibility that the scalar field parameters may vary from one BBH source to another. Similarly, it would be interesting to explore if BBH observations can be used to determine or constrain the mass of ultralight bosons. We plan to pursue these prospects in a future work.

ACKNOWLEDGMENTS

We are thankful to Cristiano Palomba and the referee for their useful comments and suggestions. This research is supported by the Spanish Agencia Estatal de Investigación (Grant No. PGC2018-095984-B-I00), by the Generalitat Valenciana (PROMETEO/2019/071), by the European Unions Horizon 2020 RISE programme H2020-MSCA-RISE-2017 (Grant No. FunFiCO-777740), and by DGAPA-UNAM through Grant No. IN105920. A. G. is supported, in part, by the Navajbai Ratan Tata Trust research grant. N. S.-G. is supported by the Fundação para a Ciência e a Tecnologia (FCT) Projects No. PTDC/FIS-OUT/28407/2017, UID/FIS/00099/2020 (CENTRA), and CERN/FIS-PAR/0027/2019. The numerical simulations for this work were performed on the Perseus and Pegasus clusters, which are part of the high performance computing facility at The Inter-University Centre for Astronomy and Astrophysics, Pune, India. We would also like to acknowledge the help and support of their staff.

APPENDIX A: CONSTRAINT VIOLATION IN THE PRESENCE OF A SCALAR FIELD

As described in Sec. III A, the introduction of a scalar-field distribution in an otherwise constraint-preserving BBH initial setup leads to constraint violations. To make sure that our numerical simulations are still valid for the time evolution under consideration, we compute the changes in the mass and area of the black hole and compare these values with the no-scalar-field scenario.

Figure 10 shows the percentage change in mass (top) and the corresponding change in area (bottom) for the largest mass parameter considered, $\tilde{\mu} = 0.8$, and for three values of the field strength.

To compute the area, mass, and other physical quantities on the horizon, we first find the horizon using the AHFinderDirect thorn [75,76] and then apply the QuasiLocalMeasures thorn, which implements the isolated and dynamical horizon framework [101–103]. This framework enables the computation of quasilocal quantities on marginally trapped surfaces such as the apparent horizon. Recently, the correlation between the shear of the horizon and the news function in the wave zone was demonstrated for quasicircular BBH mergers [104,105], and horizon dynamics was studied in terms of the shear and multipole moments for the head-on collision of two black holes [106]. These works could be important steps toward inferring finer details of black hole horizon properties through gravitational-wave observations. It might be interesting to pursue similar studies in the presence of scalar field clouds, which we aim to do in the future.

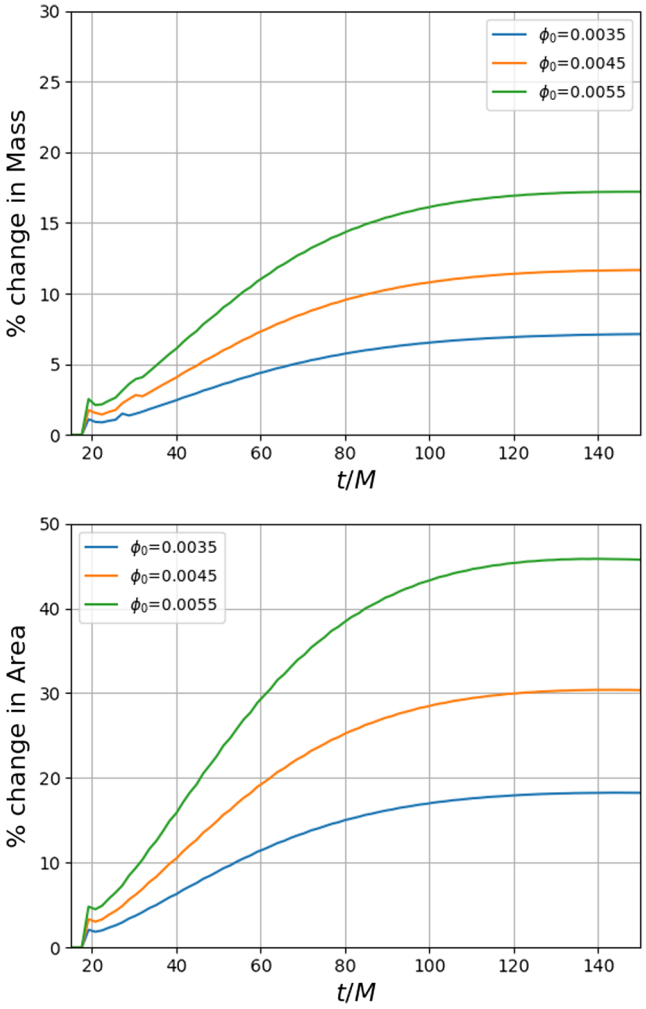

FIG. 10. Percentage change in mass (top panel) and area (bottom panel) with respect to the no-scalar-field case for the largest mass parameter considered, $\tilde{\mu} = 0.8$, and for the field strengths $\phi_0 = 3.5 \times 10^{-3}$, 4.5×10^{-3}, and 5.5×10^{-3}.

In Fig. 11 we show the evolution of the L_2 norm of the Hamiltonian constraint for the simulations of Fig. 10. We find that the magnitude of the violation of the L_2 norm of the Hamiltonian constraint is comparable to the no-scalar-field case for the range of field strengths ϕ_0 and mass parameter $\tilde{\mu}$ considered. We note that since these results correspond to the largest mass parameter of our study, the impact of the constraint violation is in general much lower for the ϕ_0-$\tilde{\mu}$ parameter space investigated.

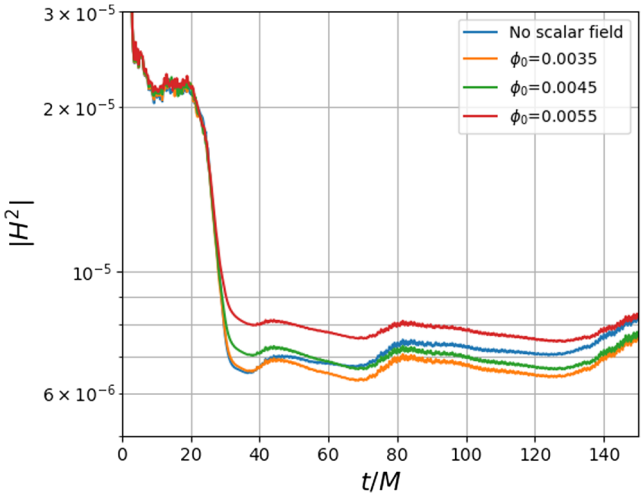

FIG. 11. Time evolution of the L_2 norm of the Hamiltonian constraint for BBH mergers with and without a scalar-field cloud. The data shown correspond to the largest mass parameter considered in this work, $\tilde{\mu} = 0.8$, for the field strengths $\phi_0 = 3.5 \times 10^{-3}$, 4.5×10^{-3}, and 5.5×10^{-3}.

APPENDIX B: PRE-PARAMETER ESTIMATION TREATMENT OF NUMERICAL DATA

Since the numerical waveforms are computed here in terms of ψ_4 as functions of time in code units of the Einstein Toolkit [71], it is necessary to convert the ψ_4 data into GW strain data and convert the code time units into seconds (physical units) so that they are usable for GW observations and parameter measurement projections. Here we show how such a conversion is done. The conversion from code units to seconds depends on the total mass of the system $M_{\rm total}$. This fact can be used to adjust the BBH mass so as to bring the frequency parameter of the numerical waveforms into aLIGO's most sensitive band, namely, 100–200 Hz.

Moreover, some care must be taken when computing the match with numerical relativity (NR) waveforms, as we explain below.

(1) The NR simulations produce ψ_4 data for our various scalar field configurations. Therefore, for GW data analysis we first construct GW strain waveforms from these data.

(2) To label the time points of the strain data in physical units we use the following conversion:

$$t(\text{in sec}) = M_{\rm total} \times \frac{M_\odot G}{c^3} * (\text{cctk\_time}), \quad \text{(B1)}$$

where cctk_time refers to the code time units in the Einstein Toolkit [71].

(3) Each waveform strain time series is chopped, resampled, and zero-padded to prepare it for our analysis with only the post-merger piece (i.e., the part of the NR waveform that starts at the time point where the peak amplitude is attained in the time domain); see Fig. 4.

(4) As we want our waveforms to be in the aLIGO sensitivity band, we choose the masses such that the frequency parameter falls in that region. To get the approximate values of those masses we calculate the match of numerical waveforms with the IMRPhenomD [97,98] template in the region (100, 200) Hz (the approximate aLIGO sensitivity band). The match comes out to be very high in the mass region of 30–60 $M_\odot$. On this basis, we choose the component masses to be 40 $M_\odot$.

(5) We also calculate the frequency of the numerical waveforms by measuring the half-cycle and conclude that we need BBHs with component masses around 40–40 $M_\odot$ each to get our frequency in the aLIGO sensitivity band.

(6) In our study we analyze numerical waveforms at different source distances. We do this by making the peak amplitude of numerical waveforms equal to the PyCBC-generated IMRPhenomD template for the distance we want to study [107].

[1] B. P. Abbott, R. Abbott, T. D. Abbott, S. Abraham, F. Acernese, K. Ackley, C. Adams, and R. e. a. Adhikari (LIGO Scientific Collaboration, and Virgo Collaboration), Phys. Rev. X **9**, 031040 (2019).
[2] gracedb.ligo.org
[3] R. Abbott *et al.* (LIGO Scientific Collaboration and Virgo Collaboration), Phys. Rev. D **102**, 043015 (2020).
[4] B. Abbott *et al.* (LIGO Scientific, Virgo), Astrophys. J. Lett. **892**, L3 (2020).
[5] R. Abbott *et al.*, Astrophys. J. Lett. **896**, L44 (2020).
[6] R. Abbott, others, LIGO Scientific Collaboration, and Virgo Collaboration, Phys. Rev. Lett. **125**, 101102 (2020).
[7] B. Abbott *et al.* (LIGO Scientific, Virgo), Astrophys. J. Lett. **900**, L13 (2020).
[8] S. L. Liebling and C. Palenzuela, Living Rev. Relativity **15**, 6 (2012).
[9] L. K. Wong, A.-C. Davis, and R. Gregory, Phys. Rev. D **100**, 024010 (2019).
[10] N. Guerlebeck and M. Scholtz, Phys. Rev. D **97**, 084042 (2018).

[11] M. A. Sedda *et al.*, Class. Quantum Grav. **37**, 215011 (2020).
[12] S. Aneesh, S. Bose, and S. Kar, Phys. Rev. D **97**, 124004 (2018), arXiv:1803.10204.
[13] V. Cardoso and P. Pani, Living Rev. Relativity **22**, 4 (2019).
[14] C. Palenzuela, I. Olabarrieta, L. Lehner, and S. L. Liebling, Phys. Rev. D **75**, 064005 (2007).
[15] V. Cardoso, S. Hopper, C. F. Macedo, C. Palenzuela, and P. Pani, Phys. Rev. D **94**, 084031 (2016).
[16] R. Brito, V. Cardoso, and H. Okawa, Phys. Rev. Lett. **115**, 111301 (2015).
[17] R. Brito, V. Cardoso, C. F. Macedo, H. Okawa, and C. Palenzuela, Phys. Rev. D **93**, 044045 (2016).
[18] T. Helfer, E. A. Lim, M. A. Garcia, and M. A. Amin, Phys. Rev. D **95**, 124005 (2019).
[19] M. Bezares, C. Palenzuela, and C. Bona, Phys. Rev. D **95**, 124005 (2017).
[20] C. Palenzuela, P. Pani, M. Bezares, V. Cardoso, L. Lehner, and S. Liebling, Phys. Rev. D **96**, 104058 (2017).
[21] T. Dietrich, S. Ossokine, and K. Clough, Class. Quantum Grav. **36**, 025002 (2019).
[22] K. Clough, T. Dietrich, and J. C. Niemeyer, Phys. Rev. D **98**, 083020 (2018).
[23] M. Bezares and C. Palenzuela, Classical Quantum Gravity **35**, 234002, (2018).
[24] N. Sanchis-Gual, C. Herdeiro, J. A. Font, E. Radu, and F. Di Giovanni, Phys. Rev. D **99**, 024017 (2019).
[25] L. Barack *et al.*, Class. Quantum Grav. **36**, 143001 (2019).
[26] A. Arvanitaki, S. Dimopoulos, S. Dubovsky, N. Kaloper, and J. March-Russell, Phys. Rev. D **81**, 123530 (2010).
[27] V. Sahni and L.-M. Wang, Phys. Rev. D **62**, 103517 (2000).
[28] W. Hu, R. Barkana, and A. Gruzinov, Phys. Rev. Lett. **85**, 1158 (2000).
[29] T. Matos and L. A. Urena-Lopez, Classical Quantum Gravity **17**, L75 (2000).
[30] T. Matos and L. A. Urena-Lopez, Phys. Rev. D **63**, 063506 (2001).
[31] L. Hui, J. P. Ostriker, S. Tremaine, and E. Witten, Phys. Rev. D **95**, 043541 (2017).
[32] H. Witek, V. Cardoso, A. Ishibashi, and U. Sperhake, Phys. Rev. D **87**, 043513 (2013).
[33] J. Barranco, A. Bernal, J. C. Degollado, A. Diez-Tejedor, M. Megevand, M. Alcubierre, D. Núñez, and O. Sarbach, Phys. Rev. Lett. **109**, 081102 (2012).
[34] J. Barranco, A. Bernal, J. C. Degollado, A. Diez-Tejedor, M. Megevand, M. Alcubierre, D. Núñez, and O. Sarbach, Phys. Rev. D **89**, 083006 (2014).
[35] S. R. Dolan, Phys. Rev. D **87**, 124026 (2013).
[36] A. Cruz-Osorio, F. S. Guzman, and F. D. Lora-Clavijo, J. Cosmol. Astropart. Phys. 06 (**2011**) 029.
[37] N. Sanchis-Gual, J. C. Degollado, P. J. Montero, and J. A. Font, Phys. Rev. D **91**, 043005 (2015).
[38] N. Sanchis-Gual, J. C. Degollado, P. J. Montero, J. A. Font, and V. Mewes, Phys. Rev. D **92**, 083001 (2015).
[39] N. Sanchis-Gual, J. C. Degollado, P. Izquierdo, J. A. Font, and P. J. Montero, Phys. Rev. D **94**, 043004 (2016).
[40] N. Sanchis-Gual, J. C. Degollado, P. J. Montero, J. A. Font, and C. Herdeiro, Phys. Rev. Lett. **116**, 141101 (2016).
[41] S. Detweiler, Phys. Rev. D **22**, 2323 (1980).
[42] S. R. Dolan, Phys. Rev. D **76**, 084001 (2007).
[43] R. Brito, V. Cardoso, and P. Pani, *Superradiance*, Lecture Notes in Physics, Vol. 906 (Springer, Cham, 2015).
[44] W. E. East and F. Pretorius, Phys. Rev. Lett. **119**, 041101 (2017).
[45] W. E. East, Phys. Rev. D **96**, 024004 (2017).
[46] W. E. East, F. M. Ramazanoğlu, and F. Pretorius, Phys. Rev. D **89**, 061503 (2014).
[47] H. Okawa, Classical Quantum Gravity **32**, 214003 (2015).
[48] C. A. Herdeiro and E. Radu, Phys. Rev. Lett. **112**, 221101 (2014).
[49] C. Herdeiro and E. Radu, Classical Quantum Gravity **32**, 144001 (2015).
[50] A. Arvanitaki, M. Baryakhtar, S. Dimopoulos, S. Dubovsky, and R. Lasenby, Phys. Rev. D **95**, 043001 (2017).
[51] R. Brito, S. Ghosh, E. Barausse, E. Berti, V. Cardoso, I. Dvorkin, A. Klein, and P. Pani, Phys. Rev. D **96**, 064050 (2017).
[52] Q. Yang, L.-W. Ji, B. Hu, Z.-J. Cao, and R.-G. Cai, Res Astron. Astrophys. **18**, 065 (2018).
[53] C. Palomba, S. D'Antonio, P. Astone, S. Frasca, G. Intini, I. La Rosa, P. Leaci, S. Mastrogiovanni, A. L. Miller, F. Muciaccia, O. J. Piccinni, L. Rei, and F. Simula, Phys. Rev. Lett. **123**, 171101 (2019).
[54] D. Baumann, H. S. Chia, and R. A. Porto, Phys. Rev. D **99**, 044001 (2019).
[55] L. Sun, R. Brito, and M. Isi, Phys. Rev. D **101**, 063020 (2020).
[56] N. Siemonsen and W. E. East, Phys. Rev. D **101**, 024019 (2020).
[57] S. Ghosh, E. Berti, R. Brito, and M. Richartz, Phys. Rev. D **99**, 104030 (2019).
[58] M. Isi, L. Sun, R. Brito, and A. Melatos, Phys. Rev. D **99**, 084042 (2019).
[59] K. K. Y. Ng, M. Isi, C.-J. Haster, and S. Vitale, Phys. Rev. D **102**, 083020 (2020).
[60] J. C. Bustillo, N. Sanchis-Gual, A. Torres-Forné, J. A. Font, A. Vajpeyi, R. Smith, C. Herdeiro, E. Radu, and S. H. Leong, arXiv:2009.05376.
[61] H. Okawa, H. Witek, and V. Cardoso, Phys. Rev. D **89**, 104032 (2014).
[62] J. Barranco, A. Bernal, J. C. Degollado, A. Diez-Tejedor, M. Megevand, M. Alcubierre, D. Nunez, and O. Sarbach, Phys. Rev. Lett. **109**, 081102 (2012).
[63] J. Barranco, A. Bernal, J. C. Degollado, A. Diez-Tejedor, M. Megevand, M. Alcubierre, D. Nez, and O. Sarbach, Phys. Rev. D **89**, 083006 (2014).
[64] J. Barranco, A. Bernal, J. C. Degollado, A. Diez-Tejedor, M. Megevand, M. Alcubierre, D. Nunez, and O. Sarbach, Phys. Rev. D **84**, 083008 (2011).
[65] T. Nakamura, K. Oohara, and Y. Kojima, Prog. Theor. Phys. Suppl. **90**, 1 (1987).
[66] M. Shibata and T. Nakamura, Phys. Rev. D **52**, 5428 (1995).
[67] T. W. Baumgarte and S. L. Shapiro, Phys. Rev. D **59**, 024007 (1998).
[68] M. Alcubierre, G. Allen, B. Brügmann, T. Dramlitsch, J. A. Font, P. Papadopoulos, E. Seidel, N. Stergioulas, W.-M. Suen, and R. Takahashi, Phys. Rev. D **62**, 044034 (2000).

[69] M. Alcubierre, B. Brügmann, P. Diener, M. Koppitz, D. Pollney, E. Seidel, and R. Takahashi, Phys. Rev. D **67**, 084023 (2003).
[70] F. Löffler, J. Faber, E. Bentivegna, T. Bode, P. Diener, R. Haas, I. Hinder, B. C. Mundim, C. D. Ott, E. Schnetter, G. Allen, M. Campanelli, and P. Laguna, Classical Quantum Gravity **29**, 115001 (2012).
[71] EinsteinToolkit, Einstein Toolkit: Open software for relativistic astrophysics (ET_2019_03 "proca, released 2019-03-29),".
[72] M. Zilhão and F. Löffler, Int. J. Mod. Phys. A **28**, 1340014 (2013).
[73] E. Schnetter, S. H. Hawley, and I. Hawke, Classical Quantum Gravity **21**, 1465 (2004).
[74] Carpet, http://www.carpetcode.org/, Carpet: Adaptive Mesh Refinement for the Cactus Framework.
[75] J. Thornburg, Classical Quantum Gravity **21**, 743 (2004).
[76] J. Thornburg, Phys. Rev. D **54**, 4899 (1996).
[77] J. D. Brown, P. Diener, O. Sarbach, E. Schnetter, and M. Tiglio, Phys. Rev. D **79**, 044023 (2009).
[78] H. Witek, M. Zilhao, G. Ficarra, and M. Elley, Canuda: a public numerical relativity library to probe fundamental physics (2020).
[79] M. Zilhao, H. Witek, and V. Cardoso, Classical Quantum Gravity **32**, 234003 (2015).
[80] N. Sanchis-Gual, F. Di Giovanni, M. Zilhão, C. Herdeiro, P. Cerdá-Durán, J. Font, and E. Radu, Phys. Rev. Lett. **123**, 221101 (2019).
[81] F. Di Giovanni, N. Sanchis-Gual, P. Cerdá-Durán, M. Zilhão, C. Herdeiro, J. A. Font, and E. Radu, Phys. Rev. D **102**, 124009 (2020).
[82] J. M. Bowen and J. W. York, Phys. Rev. D **21**, 2047 (1980).
[83] J. York, in *Frontiers in Numerical Relativity*, edited by C. Evans, L. Finn, and D. Hobill (Cambridge University Press, Cambridge, England, 1989) pp. 89–109.
[84] B. Bruegmann *et al.*, Phys. Rev. D **77**, 024027 (2008).
[85] M. Hannam, S. Husa, D. Pollney, B. Brugmann, and N. O'Murchadha, Phys. Rev. Lett. **99**, 241102 (2007).
[86] M. Ansorg, B. Brügmann, and W. Tichy, Phys. Rev. D **70**, 064011 (2004).
[87] J. G. Baker, M. Campanelli, C. O. Lousto, and R. Takahashi, Phys. Rev. D **65**, 124012 (2002).
[88] G. B. Cook, Phys. Rev. D **50**, 5025 (1994).
[89] E. Newman and R. Penrose, J. Math. Phys. **3**, 566 (1962).
[90] Gravitational Wave postprocessing tool pyGWAnalysis: "svn.einsteintoolkit.org/pyGWAnalysis/trunk", http://einsteintoolkit.org/.
[91] J. Aasi *et al.* (LIGO Scientific, VIRGO), Phys. Rev. D **89**, 102006 (2014).
[92] D. Talukder, E. Thrane, S. Bose, and T. Regimbau, Phys. Rev. D **89**, 123008 (2014).
[93] S. Bose, S. Dhurandhar, A. Gupta, and A. Lundgren, Phys. Rev. D **94**, 122004 (2016).
[94] G. Ashton, M. Hübner, P. D. Lasky, C. Talbot, K. Ackley, S. Biscoveanu, Q. Chu, A. Divakarla, P. J. Easter, B. Goncharov, F. H. Vivanco, J. Harms, M. E. Lower, G. D. Meadors, D. Melchor, E. Payne, M. D. Pitkin, J. Powell, N. Sarin, R. J. E. Smith, and E. Thrane, Astrophys. J. Suppl. Ser. **241**, 27 (2019).
[95] J. S. Speagle, Mon. Not. R. Astron. Soc. **493**, 3132 (2020).
[96] J. Skilling, in *American Institute of Physics Conference Series, American Institute of Physics Conference Series*, Vol. 735, edited by R. Fischer, R. Preuss, and U. V. Toussaint (AIP Publishing, Garching, 2004) pp. 395–405.
[97] S. Husa, S. Khan, M. Hannam, M. Pürrer, F. Ohme, X. J. Forteza, and A. Bohé, Phys. Rev. D **93**, 044006 (2016).
[98] S. Khan, S. Husa, M. Hannam, F. Ohme, M. Pürrer, X. J. Forteza, and A. Bohé, Phys. Rev. D **93**, 044007 (2016).
[99] A. L. anticipated Sensitivity curves, https://dcc.ligo.org/LIGO-T0900288/public.
[100] D. Talukder, S. Bose, S. Caudill, and P. T. Baker, Phys. Rev. D **88**, 122002 (2013).
[101] O. Dreyer, B. Krishnan, D. Shoemaker, and E. Schnetter, Phys. Rev. D **67**, 024018 (2003).
[102] A. Ashtekar and B. Krishnan, Living Rev. Relativity **7**, 10 (2004).
[103] E. Schnetter, B. Krishnan, and F. Beyer, Phys. Rev. D **74**, 024028 (2006).
[104] A. Gupta, B. Krishnan, A. Nielsen, and E. Schnetter, Phys. Rev. D **97**, 084028 (2018).
[105] V. Prasad, A. Gupta, S. Bose, B. Krishnan, and E. Schnetter, Phys. Rev. Lett. **125**, 121101 (2020).
[106] P. Mourier, X. Jimenez-Forteza, D. Pook-Kolb, B. Krishnan, and E. Schnetter, arXiv:2010.15186.
[107] A. Nitz, I. Harry, D. Brown, C. M. Biwer, J. Willis, T. D. Canton, C. Capano, L. Pekowsky, T. Dent, A. R. Williamson, G. S. Davies, S. De, M. Cabero, B. Machenschalk, P. Kumar, S. Reyes, D. Macleod, F. Pannarale, dfinstad, T. Massinger, M. Tpai, L. Singer, S. Khan, S. Fairhurst, S. Kumar, A. Nielsen, SSingh087, shasvath, I. Dorrington, and B. U. V. Gadre, gwastro/pycbc: Pycbc release v1.16.7 (2020).